Supporting Information

Risca et al. 10.1073/pnas.1114292109

SI Materials and Methods

Proteins. Actin was purified from rabbit skeletal muscle (1) and labeled on thiol groups with Alexa Fluor 546-C5-maleimide (AF546; Invitrogen), Alexa Fluor 488-C5-maleimide (AF488; Invitrogen), or maleimide-PEO$_2$-biotin (Pierce, Thermo Fisher Scientific). It was labeled on primary amines using Alexa Fluor 488 sulfodicholorphenol ester (Invitrogen) and Cy3 N-Hydroxy-succinimide (NHS) (GE Healthcare). Rabbit skeletal muscle actin biotinylated on random lysines was purchased (Cytoskeleton). Actin-related protein (Arp) 2/3 complex was purified from bovine brain as described (2) or purchased (Cytoskeleton). The (His)$_6$-tagged WCA domain of rat neural Wiskott–Aldrich syndrome protein δEVH1, a kind gift from D. Wong and J. Taunton (University of California, San Francisco), was expressed in *Escherichia coli* BL21 DE3 RIL and purified by affinity chromatography as described previously (2).

Modified Branching Assays. For branching assays with phalloidin-stabilized mother filaments, 5 μM G-actin (10% biotinylated) and 5 μM rhodamine-phalloidin (Sigma-Aldrich), were copolymerized by adding 1/10 volume of 10× KMEI buffer (500 mM KCl, 10 mM MgCl$_2$, 10 mM EGTA, 100 mM imidazole, pH 7.0) with 1 mM ATP at 23 °C in the dark for 1 h and the resulting phalloidin-F-actin was stored at 23 °C in the dark for 3–16 h. This stock was diluted to 50 nM in KMEI (50 mM KCl, 1 mM MgCl$_2$, 1 mM EGTA, 10 mM imidazole, pH 7.0) and incubated in the flow channel 6–8 min. The branch nucleation mix in this case contained unlabeled G-actin and was washed out with KMEI containing 1 μM AF488-phalloidin (Invitrogen), then KMEI containing oxygen scavenger.

For branch stability experiments, the branching mix was replaced with debranching buffer containing KMEI, unlabeled and unstabilized F-actin to prevent depolymerization, and 2 mg/mL BSA to prevent branches from adsorbing to the surface. Each surface was then incubated for 33 min to allow debranching to take place and imaged during the incubation. To obtain curvature distributions, identical samples were prepared and incubated with debranching buffer for 50 s (the minimum time possible, due to washes) or 15 min before stabilization with phalloidin and imaging.

Imaging and Image Processing. Filaments were imaged using a spinning disk confocal microscope (Axiovert; Carl Zeiss AG) (Solamere Technology Group; 491 and 561 nm lasers) with an EMCCD camera (Cascade II, Photometrics), a 63×, 1.4 N.A. oil-immersion objective (Carl Zeiss), and MetaMorph software (Molecular Devices). Red channel images were threshholded, median-filtered with a filter radius of one pixel, and skeletonized to eight-connected digital curves using ImageJ. Curves that intersected were split by removing one pixel at the intersection point.

Curvature Estimation, Spline Method. We reanalyzed the unstabilized, maleimide-labeled actin data with a cubic spline-based method of curvature estimation, which is prone to more systematic error than the tangent angle method but provides an independent check on systematic errors inherent to the tangent angle-based method (3, 4). All automated curvature analysis was done using custom-written routines in MATLAB. The eight-connected digital curves were then traced and reparameterized in terms of the chord length t, an approximation for the arc length s. Cubic splines $(x(t), y(t))$ were then fit to the digital curves using a least-squares algorithm weighted by the intensity of the digital curve's

corresponding pixels in the original gray-scale image. The distance (in pixels) between knots (polynomial join sites in the splines) was 10 pixels. Digital curves with less than 11 pixels were ignored in the analysis. Curvature was measured at points 1.1 pixels apart along the filament curve by applying the definition of curvature

$$\kappa = \frac{x'y'' - y'x''}{(x'^2 + y'^2)^{3/2}}, \qquad \text{[S1]}$$

where all derivatives are with respect to t. The first and last two pixels of each digital curve were ignored to avoid end effects.

Statistics. Each independent experiment consisted of at least 30 (usually 60) fields of view, and only experiments with 500 or more branches for which local curvature could be assigned were used (with about 2,000 branches and 12 mm of filaments each, on average). To strictly satisfy the assumptions of linear regression and the Kolmogorov–Smirnov test, relative linear branch density was calculated from a subset of mother filament curvature points randomly chosen, one per filament. These data were fit in two ways: They were either pooled, or fit individually for each experiment, such that the extracted slope and intercept from each independent experiment could be then pooled and analyzed using a one-sample t test or a one-sample Wilcoxon signed-rank test (Table S2). In all cases, linear regression was performed using weighted least squares, with the number of mother filament samples in each bin serving as the weight for each point, in order to compensate for unequal variance between low and high curvature data. The slope of the trend line from experiments performed under different conditions was compared using ANCOVA for the least-squared fits to pooled data, or a two-sample Welch's t test or a nonparametric two-sample Wilcoxon signed-rank test (also known as a Mann–Whitney test) for the slopes calculated from individual experiment line fits (Table S3). A two-sample Kolmogorov–Smirnov test was used to ask whether mother filament curvature samples and branch curvatures are drawn from the same distribution (Table S1). In all cases, $\alpha = 0.05$ and all p values reported are for two-tailed hypothesis tests. Statistical calculations were performed using R.

Monte Carlo Sampling of Worm-Like Chain (WLC) Filament Conformations. F-actin was coarse-grained as a discretized WLC polymer composed of 5.4-nm-long bonds between particles, approximately the size of an actin monomer (5) (Fig. S6), with a persistence length of 9 μm (6). In order to mimic the tethering of actin filaments to a plane surface in experiments, we restrict Monte Carlo moves to certain sections of the 1.25-μm-long filament, effectively pinning down the filament at six equally spaced points. The Monte Carlo moves consist of attempts to perform a crankshaft move. A crankshaft move involves rotating two randomly selected particles i and j and all the particles in between by a random angle around the line segment that connects particles i and j (7). Conformations are sampled with the Metropolis acceptance criterion,

$$P_{\text{acc}} = \min[1, e^{-\beta \Delta E}] \qquad \text{[S2]}$$

where $\beta = 1/k_B T$ and WLC bending energy

$$E = E_{\text{bending}} = k_B T \frac{l_p}{2} \int_0^L \left| \frac{d^2 \vec{r}(s)}{ds^2} \right| ds, \qquad \text{[S3]}$$

where L is the contour length of the polymer, l_p is its persistence length, and $\vec{r}(s)$ is the position of the polymer at arc length coordinate s (8). Robustness analysis was performed to examine the effect of changing various simulation parameters on the distribution of local curvatures. The parameters considered were (*i*) length between adjacent particles, (*ii*) contour length of filament between tether points, (*iii*) "looseness," the ratio of end-to-end length to contour length between tether points, (*iv*) number of tethers, and (*v*) curvature resolution and the possible need to average curvature over neighboring angles. These test simulations revealed that only averaging over neighboring angles has a significant effect on curvature distributions. The final set of parameters employed for the simulations is 5.4 nm between adjacent particles, a contour length of 250 nm between tether points, the end-to-end length between tether points for a given contour length equal to the average end-to-end distance $\langle R \rangle$ for a free WLC polymer of the same persistence length and contour length, as given by

$$\langle R \rangle = \sqrt{2l_p L \left[1 - \frac{l_p}{L} \left(1 - e^{-L/l_p} \right) \right]}, \qquad \textbf{[S4]}$$

and no averaging of the local curvature. Curvature of the WLC polymer, κ, was calculated from the angle between successive bonds, θ, and the length of the bonds, Δs (Fig. S6):

$$\kappa = \sqrt{\frac{2}{(\Delta s)^2} (1 - \cos \theta)}. \qquad \textbf{[S5]}$$

This definition of curvature is equivalent to a discretization of Eq. **S1**. The key difference between continuous and discrete measures of curvature is that, in the discrete case, the increment of arc length, Δs, must have a nonzero value, which has a strong effect on the value of the curvature measured. Counterintuitively, even though a discretized WLC polymer is stiff on short length scales, it can have large curvature fluctuations on those scales because the polymer's small fluctuations in θ, the bending angle, are divided by a small Δs. These scale effects motivated our use of Monte Carlo simulations to make a connection between the length scale observable by light microscopy and the length scale of the Arp2/3 complex.

Projection of 3D Curvature onto 2D. Imposed curvatures were largely in a 2D plane because filaments were tethered to the coverslip surface and their stiffness limited out-of-plane bending of large amplitude. Filament ends and large loops that were not tethered were blurred during the 1-s exposures used, and were eliminated during image thresholding. To approximate the experimental conditions, the WLC filament was simulated in three dimensions, but tethered to a 2D plane and curvature was measured in 2D from the projection of the filaments' shape onto that plane, neglecting out-of-plane bending. For consistency, 2D projection was used for all curvature analysis of filament shape in experiments and simulations, as well as for determination of branch direction. The reported relative linear branch density also contained an internal control, as branching from curved filament sections can be compared directly to branching from straight filament sections.

1. Spudich JA, Watt S (1971) The regulation of rabbit skeletal muscle contraction. I. Biochemical studies of the interaction of the tropomyosin-troponin complex with actin and the proteolytic fragments of myosin. *J Biol Chem* 246:4866–4871.
2. Egile C, et al. (1999) Activation of the CDC42 effector N-WASP by the Shigella flexneri IcsA protein promotes actin nucleation by Arp2/3 complex and bacterial actin-based motility. *J Cell Biol* 146:1319–1332.
3. Worring M, Smeulders AWM (1993) Digital curvature estimation. *CVGIP Imag Understan* 58:366–382.
4. Bicek AD, Tüzel E, Kroll DM, Odde DJ (2007) Analysis of microtubule curvature. *Methods Cell Biol* 83:237–268.
5. Rouiller I, et al. (2008) The structural basis of actin filament branching by the Arp2/3 complex. *J Cell Biol* 180:887–895.
6. Isambert H, et al. (1995) Flexibility of actin filaments derived from thermal fluctuations. Effect of bound nucleotide, phalloidin, and muscle regulatory proteins. *J Biol Chem* 270:11437–11444.
7. Ullner M, Staikos G, Theodorou DN (1998) Monte Carlo simulations of a single polyelectrolyte in solution: Activity coefficients of the simple ions and application to viscosity measurements. *Macromolecules* 31:7921–7933.
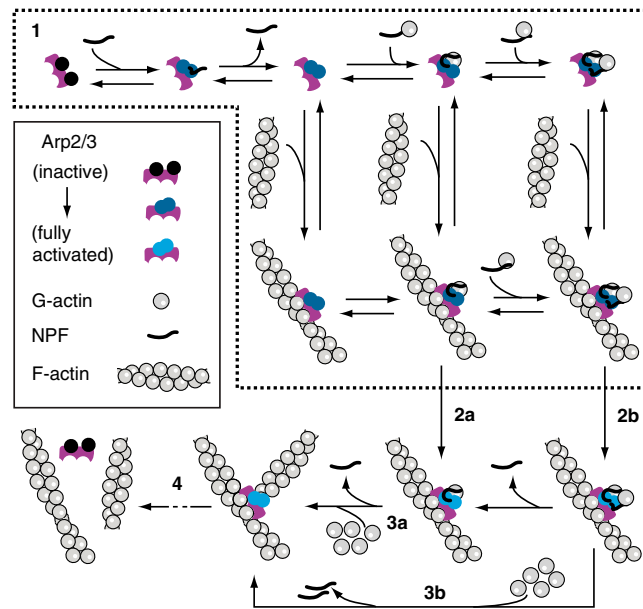8. Doi M, Edwards SF (2001) The Theory of Polymer Dynamics (Clarendon, Oxford).

Fig. S1. Arp2/3 branch nucleation occurs via a complex pathway (1–12). (*1*) The Arp2/3 complex (violet and shades of blue), one or two molecules of nucleation-promoting factor (NPF, black curve), and one or two G-actin monomers (gray), assemble on a preexisting F-actin "mother" filament (gray). Interaction with the NPF causes a conformational change in the inactive Arp2/3 complex (violet and black) that partially activates it, bringing Arp2 and Arp3 into a conformation similar to a short-pitch helix actin dimer (violet and dark blue). There are multiple pathways for assembly of this complex, and the extent to which different pathways are populated in vivo remains to be elucidated. (*2a* and *2b*) The mother filament bound Arp2/3 complex then undergoes a further conformational change that fully activates the Arp2/3 complex (violet and light blue) for nucleation of a new actin filament as a branch on the mother filament. (*3a* and *3b*) This new filament then elongates as more actin monomers bind to its free barbed end, and the NPF dissociates soon after nucleation. (*4*) After several minutes, the two filaments dissociate in a process called debranching.

1 Beltzner CC, Pollard TD (2008) Pathway of actin filament branch formation by Arp2/3 complex. *J Biol Chem* 283:7135–7144.
2 Padrick SB, Doolittle LK, Brautigam CA, King DS, Rosen MK (2011) Arp2/3 complex is bound and activated by two WASP proteins. *Proc Natl Acad Sci USA* 108:E472–E479.
3 Pollard TD (2007) Regulation of actin filament assembly by Arp2/3 complex and formins. *Annu Rev Biophys Biomol Struct* 36:451–477.
4 Ti S, Jurgenson CT, Nolen BJ, Pollard TD (2011) Structural and biochemical characterization of two binding sites for nucleation-promoting factor WASp-VCA on Arp2/3 complex. *Proc Natl Acad Sci USA* 108:E463–E471.
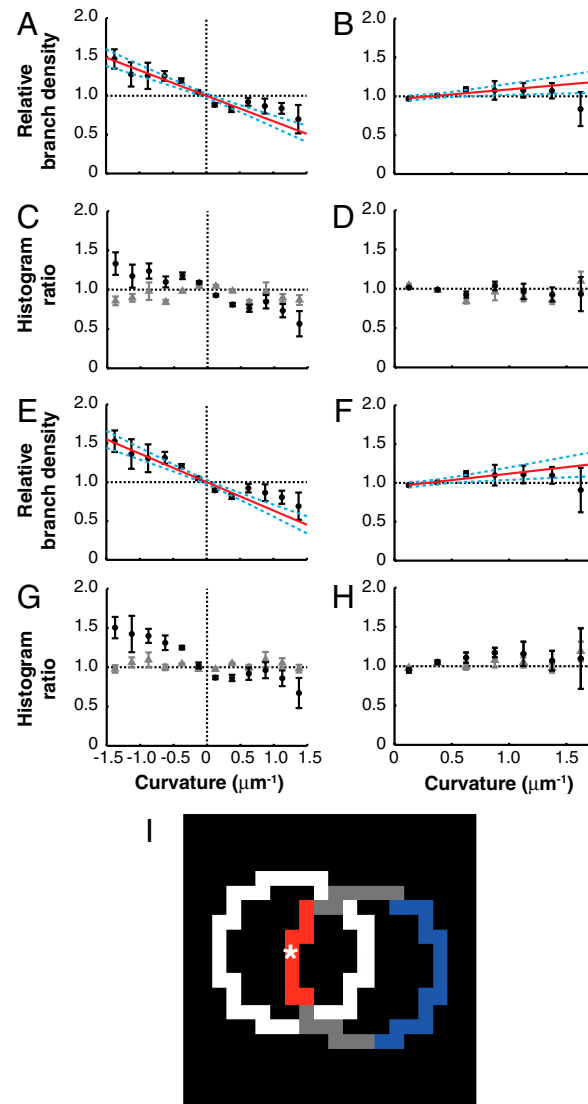
Fig. S2. Quantification of the curvature dependence of branching. A subset of the data in Fig. 2, with curvature estimated by the tangent angle method, was used to assemble histograms and relative branch density curves from uncorrelated curvature samples. The signed and unsigned mother filament curvature distribution was measured by sampling the curvature of mother filaments at only one randomly chosen point (away from the ends) on each filament (see *SI Materials and Methods*). This sampling method was used to avoid correlations between curvature points collected at nearby locations on the same filament. Relative linear branch density is shown as a function of (*A*) signed and (*B*) unsigned curvature. These measurements of the linear branch density, based on independent samples, satisfy the assumptions of linear regression and were used to estimate the magnitude of the linear trends in branch density with curvature. The results of a weighted least-squares regression on pooled data are shown as the line of means (red line) and the 95% confidence interval on the line of means (cyan, dashed lines) (Table S2). *C* and *D* show the raw histogram ratios used to calculate branch density (black circles) and the ratios calculated from randomly generated branches along the same set of mother filament curves, analyzed identically and used to correct the branch density data for systematic errors introduced by bias in the curvature estimation method (gray triangles). (*E*–*H*) Similar plots describing the same set of experiments analyzed by making many curvature measurements on each filament. Data shown in *E* and *F* are identical to Fig. 2*D* and *H*. (*I*) For a digitized circle with a radius of 5 pixels, a branch of length 5 pixels centered at * is schematically shown as a circle depicting possible locations of the branch tip, color coded as inside the circle (red), outside the circle (blue), or overlapping with the circle and having indeterminate direction. Note that more branch tip locations external to the circle are possible when the branch length is comparable to the circle radius, introducing a curvature-dependent systematic error into our measurement. Such errors were compensated for by subtracting the simulated random branch density (gray triangles in *C*, *D*, *G*, and *H*) from the real density (black circles in same plots). Error bars: SEM.
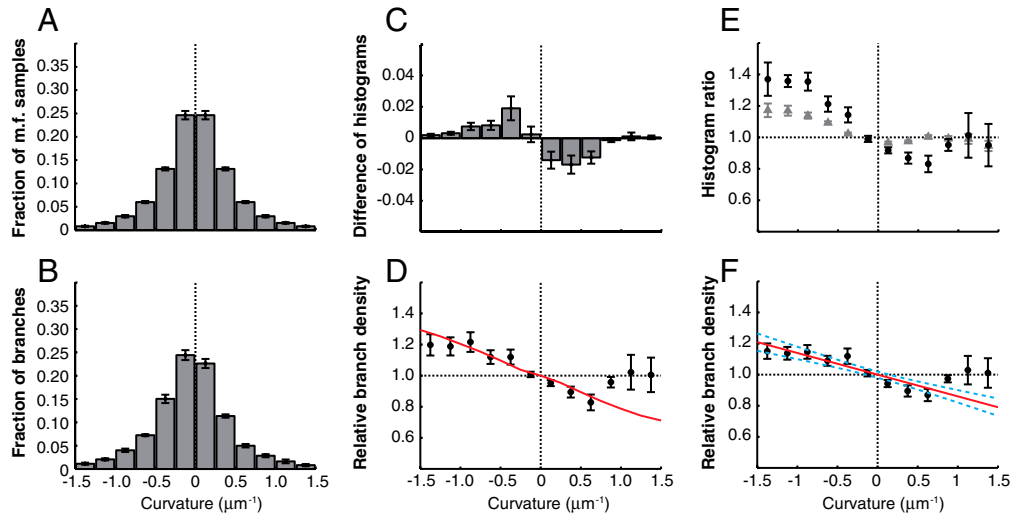
Fig. S3. Branching bias induced by curvature is also seen with spline-based curvature analysis. Raw data is the same as analyzed in Fig. 2. (*A*) Mother filament (m.f.) curvature distribution. (*B*) Distribution of curvature at branch points. (*C*) Difference of histograms in *A* and *B*. (*D*) Relative branch density as a function of curvature (gray circles) and the least-squares best-fit fluctuation gating model with a threshold curvature of 1 μm^{-1}. (*E*) Raw branch density (black circles) and control density calculated from random, simulated branches (gray triangles). The control curve was subtracted from the raw curve, experiment-by-experiment, to generate the final branch density curves averaged to generate *D*. (*F*) Subsampled data (with one curvature measurement per filament) shown with the best straight line fit (red, calculated by linear regression on the pooled data from seven experiments) and 95% confidence interval on the line of means (cyan, dashed lines). The only difference between the data shown in *D* and *F* is the set of points at which mother filament curvature was measured to sample the overall curvature distribution. Branch data and the subsequent analysis steps, including the normalization step described in *E*, are identical between *D* and *F*. Error bars: SEM.
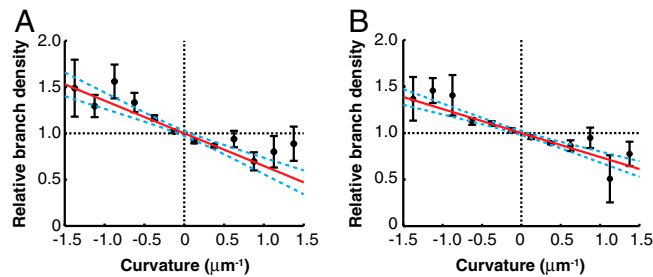
Fig. S4. The effect of image magnification on the change in relative branch density with curvature. All data were analyzed with the tangent angle-based method as in Fig. 2D. (*A*) Relative branch density of NHS-labeled mother filaments with 25 mM phosphate at 165 nm/pixel, $n = 6$ independent experiments. (*B*) Relative branch density measured from a different set of images acquired at 103 nm/pixel under the same biochemical conditions, $n = 5$. Solid red lines, linear trend fit to pooled data by least squares, weighted by the number of mother filament samples in each bin. Dotted blue lines, 95% confidence interval for the best-fit line. Error bars: SEM.
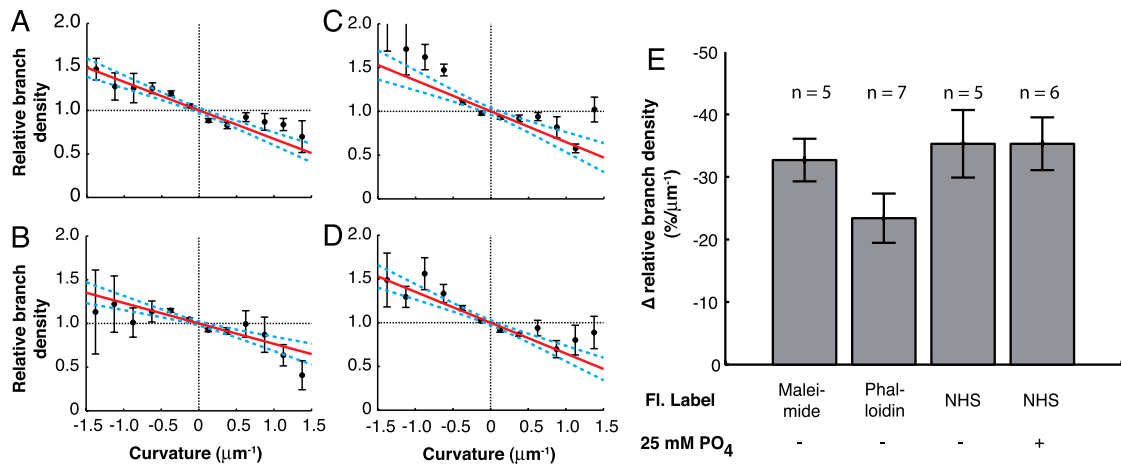
Fig. S5. Relative branch density plots and linear slope for different biochemical conditions. (*A*) Mother filaments unstabilized by phalloidin during branching, labeled with 30% maleimide-AF546 and 10% maleimide-biotin in buffer KMEI (percentages refer to fraction of labeled monomers) (see Fig. 2D, *Materials and Methods*, and *SI Materials and Methods*) (*n* = 5). (*B*) Mother filaments labeled only with 10% maleimide-biotin and stabilized with rhodamine-phalloidin during branching (*n* = 7). (*C*) Unstabilized mother filaments labeled with 30% NHS-Cy3 and 10% NHS-biotin in buffer KMEI (*n* = 5). (*D*) NHS-labeled mother filaments in buffer KMEI with 25 mM phosphate (*n* = 6). Red lines, best-fit linear slope (least squares weighted by the number of mother filament samples in each bin). Dotted blue lines, 95% confidence interval on the slope. (*E*) The slope of the relative branch density (quantification of red lines from *A–D*) shown as a function of the mode of fluorescent labeling (AF-546-maleimide or NHS-Cy3) or actin stabilization (phalloidin, phosphate, or none). All error bars: SEM.
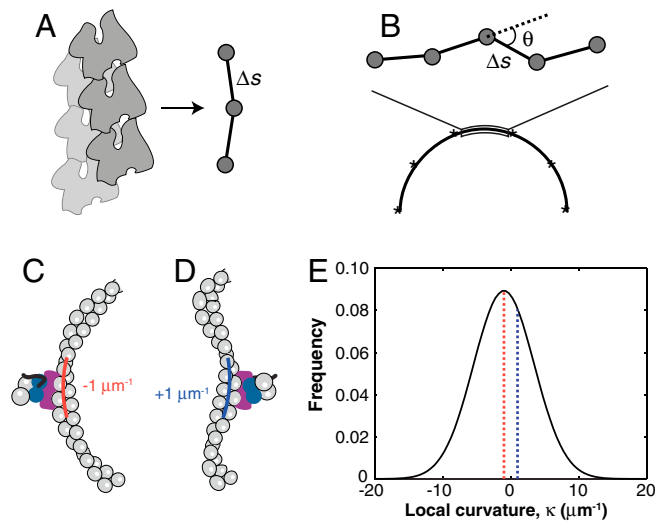

Fig. S6. The actin filament was simulated as a discretized WLC polymer. (*A*) Each particle of the WLC polymer stands for two actin monomers, with $\Delta s = 5.4$ nm bonds between particles. (*B*) The WLC polymer was tethered to a path with a defined curvature at six particles (asterisks), and curvature was calculated (*SI Materials and Methods*, Eq. **S5**), from the section between the middle two tethered particles, in order to avoid end effects. The likelihood of curvature inverting fluctuations is high because the curvature distribution is wide relative to changes in the mean, making a simple equilibrium mechanism for the branching bias unlikely. (*C*) Schematic representation of the imposed curvature (shown by red arc) of a segment of an actin filament, which is concave to the right in this case. (*D*) A shape fluctuation of the filament can transiently give rise to the same local curvature, but with opposite concavity (blue arc). A state in which the NPF- and G-actin-bound Arp2/3 complex is bound to the left side of the filament in *C* has the same energy as the ternary complex bound to the right side of the filament in *D*, because the microscopic curvature is locally the same. Therefore, the total probability of the Arp2/3 complex being bound to the right or left side of the filament depends only on the relative likelihood of states *C* and *D*. (*E*) Distribution of local curvatures on a simulated filament with imposed curvature $\kappa_0 = -1$ μm^{-1} (choosing the coordinate system arbitrarily). The average curvature does not fully describe the shape of the filament as encountered by the Arp2/3 complex. The likelihood of that location on the filament having the same local curvature as the imposed mean curvature (red line, state depicted in *C*) is only 10% larger than its likelihood having the curvature of opposite concavity, and hence opposite sign (blue line, state depicted in *D*). For comparison, the experimental results (Fig. 2) showed 99% more branching on the convex side than on the concave side.

Table S1. Two-sample, two-sided Kolmogorov–Smirnov tests to compare distribution of overall mother filament curvature and curvature at branch points for maleimide-labeled unstabilized actin in KMEI buffer

Experiment	N_{branches}	$N_{\text{MF points}}$	D	p
Signed curvature				
1	829	2,782	0.052	0.065
2	840	5,930	0.10	2.9×10^{-7}
3	3,064	8,720	0.079	1.1×10^{-12}
4	4,506	7,206	0.081	7.2×10^{-9}
5	1,204	3,226	0.081	2.0×10^{-5}
Pooled 1–5	10,443	27,864	0.068	$<2.2 \times 10^{-16}$
Unsigned curvature				
1	896	1,391	0.024	0.91
2	917	2,965	0.025	0.78
3	3,316	4,360	0.019	0.47
4	4,840	3,603	0.049	9.2×10^{-5}
5	1,310	1,613	0.020	0.94
Pooled 1–5	11,279	13,932	0.039	1.1×10^{-8}

The data used to compare distributions are drawn from the same datasets as Fig. 2, but only one mother filament curvature sample was randomly chosen from every filament to eliminate correlations between mother filament curvature samples and satisfy the assumptions underlying the Kolmogorov–Smirnov test.

Table S2. The trend of branch density change with curvature was quantified with weighted least-squares linear regression for each condition

Condition	Item for each condition	N	Stat. test method	Slope Estimate, % per μm^{-1}	Slope 95% confidence interval	p value, H_0: slope = 0	Intercept Estimate, %	Intercept 95% confidence interval	p-value (H_0: int. = 100)	R^2
Signed curvature										
Maleimide-labeled, unstabilized actin; many κ_0 samples per MF; 165 nm/pixel; tangent angle-based κ analysis	indep. exp.	5	LRPD	−37	(−44, −30)	8.3×10^{-16}	100	(97.3, 103)	0.97	0.60
	branches	10,443	OSTT	−35	(−47, −22)	0.0016	100.06	(100.03, 100.09)	0.0056	0.55
	MF samples	151,012	WSRT	−37	(−44, −17)	0.063	100.06	(100.03, 100.09)	0.063	0.55
	regression DF	72								
Maleimide-labeled, unstabilized actin; one κ_0 sample per MF; 165 nm/pixel; tangent angle-based κ analysis	indep. exp.	5	LRPD	−33	(−40, −26)	1.7×10^{-14}	100	(97.1, 103)	0.98	0.56
	branches	10,443	OSTT	−31	(−45, −17)	0.0033	100.06	(100.01, 100.11)	0.038	0.55
	MF samples	13,932	WSRT	−31	(−43, −15)	0.063	100.05	(99.998, 100.10)	0.13	0.55
	regression DF	72								
Maleimide-labeled, unstabilized actin; one κ_0 sample per MF; 165 nm/pixel; spline-based κ analysis	indep. exp.	5	LRPD	−14	(−17, −10)	3.3×10^{-12}	100	(98.1, 102)	0.99	0.40
	branches	22,580	OSTT	−12	(−22, −2.0)	0.029	100.0	(99.99, 100.0)	0.37	0.39
	MF samples	30,420	WSRT	−14	(−19, 1.8)	0.125	100.00	(100.00, 100.04)	0.44	0.39
	regression DF	97								
Maleimide-labeled actin stabilized with phalloidin; one κ_0 sample per MF; 165 nm/pixel; tangent angle-based κ analysis	indep. exp.	7	LRPD	−23	(−31, −16)	3.8×10^{-8}	100	(97.6, 102)	0.97	0.26
	branches	18,676	OSTT	−26	(−36, −16)	0.00066	100.04	(99.990, 100.09)	0.10	0.36
	MF samples	30,420	WSRT	−24	(−37, −17)	0.016	100.03	99.997, 100.09)	0.08	0.36
	regression DF	102								
NHS-labeled, unstabilized actin; one κ_0 sample per MF; 165 nm/pixel; tangent angle-based κ analysis	indep. exp.	5	LRPD	−35	(−46, −24)	7.5×10^{-9}	100.0	(96.21, 103.9)	0.98	0.37
	branches	6,042	OSTT	−37	(−47, −27)	5.7×10^{-4}	100.04	(99.982, 100.10)	0.13	0.39
	MF samples	21,468	WSRT	−38	(−48, −28)	0.063	100.04	(99.996, 100.10)	0.063	0.39
	regression DF	74								
NHS-labeled actin stabilized with 25 mM phosphate; one κ_0 sample per MF; 165 nm/pixel; tangent angle-based κ analysis	indep. exp.	6	LRPD	−35	(−44, −27)	1.6×10^{-12}	100.0	(97.30, 102.8)	0.98	0.47
	branches	9,207	OSTT	−35	(−40, −30)	1.0×10^{-5}	100.04	(99.989, 100.08)	0.11	0.53
	MF samples	16,929	WSRT	−35	(−42, −29)	0.03	100.03	(100.00, 100.11)	0.03	0.53
	regression DF	80								
NHS-labeled actin stabilized with 25 mM phosphate; one κ_0 sample per MF; 103 nm/pixel; tangent angle-based κ analysis	indep. exp.	5	LRPD	−26	(−31, −20)	2.9×10^{-14}	100.1	(98.02, 102.1)	0.94	0.54
	branches	7,473	OSTT	−26	(−32, −20)	2.8×10^{-4}	100.05	(99.961, 100.14)	0.19	0.56
	MF samples	9,085	WSRT	−26	(−32, −21)	0.063	100.05	(99.967, 100.15)	0.19	0.56
	regression DF	75								
NHS-labeled, unstabilized actin; one κ_0 sample per MF; 165 nm/pixel; tangent angle-based κ analysis; 0.83 min debranching	indep. exp.	4	LRPD	−33	(−42, −25)	2.6×10^{-10}	100.0	(97.47, 102.6)	0.98	0.54
	branches	8,552	OSTT	−37	(−58, −15)	0.012	100.01	(99.958, 100.06)	0.66	0.57
	MF samples	8,329	WSRT	−36	(−55, −23)*	0.13	100.01	(99.971, 100.05)*	0.63	0.57
	regression DF	52								

Condition	Item for each condition	N	Stat. test method	Slope Estimate, % per μm^{-1}	Slope 95% confidence interval	Slope p value, H_0:slope = 0	Intercept Estimate, %	Intercept 95% confidence interval	Intercept p-value (H_0:int. = 100)	R^2
NHS-labeled, unstabilized actin; one κ_0 sample per MF; 165 nm/pixel; tangent angle-based κ analysis; 15 min debranching	indep. exp.	4	LRPD	−31	(−40, −22)	1.1×10^{-8}	100.1	(97.22, 100.3)	0.93	0.46
	branches	5,636	OSTT	−31	(−44, −18)	0.0048	100.1	(99.93, 100.3)	0.13	0.58
	MF samples	8,581	WSRT	−36	(−42, −24)*	0.13	100.1	(99.98, 100.3)*	0.13	0.58
	regression DF	53								
Unsigned curvature										
Maleimide-labeled, unstabilized actin; many κ_0 samples per MF; 165 nm/pixel; tangent angle-based κ analysis	indep. exp.	5	LRPD	17	(6.1, 27)	0.0029	95.2	(91.0, 99.4)	0.026	0.22
	branches	11,279	OSTT	16	(−3.0, 35)	0.080	95.3	(89.6, 101)	0.089	0.25
	MF samples	151,012	WSRT	16	(−3.6, 35)	0.13	95.2	(89.2, 101)	0.13	0.25
	regression DF	37								
Maleimide-labeled, unstabilized actin; one κ_0 sample per MF; 165 nm/pixel; tangent angle-based κ analysis	indep. exp.	5	LRPD	13	(3.3, 23)	0.010	95.9	(91.8, 100)	0.053	0.17
	branches	11,279	OSTT	13	(−4.2, 30)	0.10	95.7	(90.0, 101)	0.11	0.26
	MF samples	13,932	WSRT	12	(−4.6, 29)	0.13	95.6	(89.6, 102)	0.13	0.26
	regression DF	37								
Maleimide-labeled, unstabilized actin; one κ_0 sample per MF; 165 nm/pixel; spline-based κ analysis	indep. exp.	7	LRPD	5.5	(0.92, 10)	0.020	97.7	(95.1, 100)	0.073	0.11
	branches	24,980	OSTT	8.1	(−7.0, 23)	0.21	96.4	(89.5, 103)	0.21	0.44
	MF samples	30,420	WSRT	6.1	(−9.5, 20)	0.19	96.1	(90.6, 104)	0.19	0.44
	regression DF	48								
NHS-labeled, unstabilized actin; one κ_0 sample per MF; 165 nm/pixel; tangent angle-based κ analysis	indep. exp.	5	LRPD	36	(23, 49)	2.6×10^{-6}	90.6	(85.8, 95.3)	0.00025	0.44
	branches	7,014	OSTT	40	(16, 64)	0.0098	89.5	(83.6, 95.4)	0.0077	0.52
	MF samples	21,468	WSRT	34	(26, 74)	0.063	90.6	(81.5, 93.4)	0.063	0.52
	regression DF	38								

Fitting was done on pooled data and used directly for hypothesis testing (LRPD, linear regression on pooled data; DF, degrees of freedom), or data from each experiment were individually fit, and the slopes and intercepts of the resulting best-fit lines were compared with zero using either a one-sample t test (OSTT), or the nonparametric Wilcoxon signed-rank test (WSRT). R^2 values for t test and Wilcoxon test results are averages of the R^2 values for each line fitted to data from individual experiments. (MF, mother filament; Stat. test method, statistical test method; indep. exp., independent experiments.)
*Only an 88% confidence interval could be calculated in these cases.

Table S3. Comparisons and hypothesis testing for the effects of analysis method, actin labeling method, actin stabilization, magnification, and debranching on the relative branch density trend as a function of curvature

Base condition	Change	Statistical method	Change in slope, % per μm^{-1}	95% confidence interval	p value
Maleimide-labeled, unstabilized actin; one κ_0 sample per mother filament; 165 nm/pixel; tangent angle-based curvature analysis	many κ_0 samples per mother filament	ANCOVA	−3.9	(−21, 13)	0.64
		Wilcoxon signed-rank test	−3.9	(−23, 13)	0.55
		Welch's t test	−3.7	(−19, 12)	0.60
Maleimide-labeled, unstabilized actin; one κ_0 sample per mother filament; 165 nm/pixel; tangent angle-based curvature analysis	spline-based curvature analysis	ANCOVA	19	(11, 26)	2.1×10^{-6}
		Wilcoxon signed-rank test	18	(1.2, 32)	0.031
		Welch's t test	19	(4.5, 33)	0.017
Maleimide-labeled, unstabilized actin; one κ_0 sample per mother filament; 165 nm/pixel; tangent angle-based curvature analysis	stabilization of actin with phalloidin	ANCOVA	9.3	(−1.9, 20)	0.10
		Wilcoxon signed-rank test	6.7	(−8.4, 20)	0.53
		Welch's t test	4.8	(−9.7, 19)	0.47
Maleimide-labeled, unstabilized actin; one κ_0 sample per mother filament; 165 nm/pixel; tangent angle-based curvature analysis	labeling of actin with NHS reactive esters	ANCOVA	−2.5	(−15, 10)	0.69
		Wilcoxon signed-rank test	−5.1	(−23, 11)	0.55
		Welch's t test	−5.9	(−20, 8.4)	0.37
NHS-labeled, unstabilized actin; one κ_0 sample per mother filament; 165 nm/pixel; tangent angle-based κ analysis	stabilization of actin with 25 mM phosphate	ANCOVA	−0.022	(−14, 14)	0.998
		Wilcoxon signed-rank test	2.2	(−7.1, 13)	0.79
		Welch's t test	2.1	(−8.1, 12)	0.64
NHS-labeled actin stabilized with 25 mM phosphate; one κ_0 sample per mother filament; 165 nm/pixel; tangent angle-based κ analysis	imaging at higher magnification with 103 nm/pixel	ANCOVA	9.5	(−1.0, 20)	0.076
		Wilcoxon signed-rank test	9.0	(−1.6, 23)	0.095
		Welch's t test	11	(−0.048, 0.21)	0.043
NHS-labeled, unstabilized actin; one κ_0 sample per mother filament; 165 nm/pixel; tangent angle-based κ analysis; 0.83 min debranching	extended unstabilized debranching incubation for 15 min	ANCOVA	2.8	(−9.6, 15)	0.66
		Wilcoxon signed-rank test	−5.4	(−31, 20)	0.86
		Welch's t test	−5.5	(−26, 15)	0.52

Signed curvature data was used for all comparisons.